



Article

Introduction of RKKY-pMTJ-Based Ultrafast Magnetic Sensor Architecture and Magnetic Multilayer Optimization

Jaehun Cho and June-Seo Kim *

Division of Nanotechnology, Daegu-Gyeongbuk Institute of Science and Technology (DGIST), Daegu 42988, Republic of Korea
* Correspondence: spin2mtj@dgist.ac.kr

Abstract

A state-of-the-art tunnel magnetoresistance (TMR) sensor architecture, which is based on the perpendicularly magnetized magnetic tunnel junction (pMTJ), is introduced and engineered for ultrafast, high thermal stability, and linearity for magnetic field detection. Limitations in high-frequency environments, stemming from insufficient thermal stability and slow recovery times in conventional TMR sensors, are overcome by this approach. The standard MRAM structure is modified, and the Ruderman–Kittel–Kasuya–Yosida (RKKY) interaction is employed to give a strong, internal restoring torque to the storage layer magnetization. Sensor linearity is also ensured by this RKKY mechanism, and rapid relaxation to the initial spin state is observed when an external field is removed. The structural and magnetic properties of the multilayer stack are experimentally demonstrated. Robust synthetic antiferromagnetic (SAF) coupling is confirmed by using polar MOKE spectroscopy with an optimal Ru insertion layer thickness (0.6 nm), which is essential for high thermal stability. Subsequently, an ultrafast response of this TMR sensor architecture is probed by micromagnetic simulations. The storage layer magnetization rapidly recovers to the SAF state within an ultrashort time of 5.78 to 5.99 ns. This sub-6 ns recovery time scale suggests potential operation into the hundreds of MHz range.



Academic Editor: Arcady Zhukov

Received: 2 October 2025

Revised: 29 October 2025

Accepted: 4 November 2025

Published: 6 November 2025

Citation: Cho, J.; Kim, J.-S. Introduction of RKKY-pMTJ-Based Ultrafast Magnetic Sensor Architecture and Magnetic Multilayer Optimization. *Sensors* **2025**, *25*, 6793. <https://doi.org/10.3390/s25216793>

Copyright: © 2025 by the authors. Licensee MDPI, Basel, Switzerland. This article is an open access article distributed under the terms and conditions of the Creative Commons Attribution (CC BY) license (<https://creativecommons.org/licenses/by/4.0/>).

Keywords: tunnel magnetoresistance; magnetoresistance sensor; interlayer exchange coupling; Ruderman–Kittel–Kasuya–Yosida (RKKY) interaction; micromagnetic simulations; magnetic multilayer optimization; ultrafast switching

1. Introduction

TMR (Tunnel Magneto-Resistance) sensors, characterized by exceptionally high sensitivity and low power consumption, are widely employed for the precise detection of weak magnetic fields. In the automotive sector, they are used in applications requiring high reliability, such as current sensing in electric vehicle (EV) battery systems, steering angle measurement, and wheel-speed detection in anti-lock braking systems (ABSs) [1–4]. Beyond transportation, TMR sensors play a pivotal role in smart manufacturing, where they enable precise control of motor position and angular displacement in robotic arms and automated equipment [5]. Owing to their superior performance compared to conventional Hall sensors and AMR (Anisotropic Magneto-Resistance) or GMR (Giant Magneto-Resistance) sensors, TMR sensors are rapidly expanding their influence across advanced fields that demand high-precision magnetic sensing [6].

Conventional TMR sensors typically employ CoFeB layers with thicknesses of only a few nanometers, which inherently exhibit strong in-plane magnetic anisotropy [6–8]. Con-

sequently, the magnetization of the free layer mostly rotates within the plane relative to the pinned layer, thereby modulating the tunneling currents. Since the free layer magnetization is stabilized primarily in the in-plane direction, the sensor characteristics are generally optimized for detecting in-plane magnetic fields. Such devices are commonly referred to as “in-plane magnetized MTJ sensors” (or simply “in-plane TMR sensors”) [8].

In contrast, the perpendicularly magnetized magnetic tunnel junction (pMTJ) architecture offers several significant advantages for sensor development, but practical implementation as sensor devices has remained limited due to fabrication challenges. In pMTJs, the magnetization is aligned perpendicular to the film plane (out-of-plane), which facilitates device miniaturization and high integration density while also enhancing the efficiency of spin-transfer (STT) and spin-orbit torques (SOTs). The perpendicular configuration further enables the design of response characteristics distinct from those of in-plane field sensors. Moreover, because the fabrication processes of pMTJs are largely compatible with those of magneto-resistive random-access memory (MRAM), this architecture holds strong potential for integration with semiconductor circuits [9,10]. Achieving this crucial perpendicularly magnetized structure using Perpendicular Magnetic Anisotropy (PMA) relies on specific material engineering strategies. The most common method, interfacial PMA, utilizes the strong spin-orbit coupling at the interface between a heavy metal and a ferromagnetic layer, as seen in the Pt/Co, Pd/Co structures [11–14]. Co/Pt superlattice structures are candidates for enhancing the PMA energy [15,16]. Alternatively, interface bonding with an oxide layer, such as in the highly relevant Ta/CoFeB/MgO structure, is utilized [17–19]. Alternatively, bulk PMA can be achieved by utilizing the intrinsic crystal structure of materials like L_{10} -ordered alloy, which consists of Co, Fe and Pt, Pd such as FePt or FePd alloys [20,21], which possess a large, intrinsic magnetocrystalline anisotropy suitable for high-density, thermally stable applications.

The main challenge in developing pMTJ-based TMR sensors is in the fact that the MRAM architecture cannot be directly used. Conventional MRAM structures consist of a storage layer (SL) for binary information and a reference layer (RL) with fixed magnetization. The SL thickness is optimized to maximize the magnetoresistance (MR) ratio. However, TMR sensors are always required to operate over a wide temperature range (typically -40°C to $+80^{\circ}\text{C}$), and the ultrathin SL used in MRAM shows insufficient thermal stability [22,23]. Therefore, it is difficult to ensure a sufficient retention time of the TMR sensor in a higher temperature region. To overcome this limitation, radically new MRAM architecture should be implemented for high thermal stability TMR sensor development.

In this study, we propose a modified MRAM architecture for next-generation TMR sensors. The key difference from conventional MRAM is to employ an interlayer exchange coupling (IEC), specifically the Ruderman–Kittel–Kasuya–Yosida (RKKY) interaction of appropriate strength, to stabilize the magnetization of the SL [24]. This architecture offers two major advantages: (i) under the influence of IEC or RKKY coupling, the SL acquires an angle that depends on the strength of the external magnetic field, thereby ensuring linearity in the TMR sensor response; and (ii) when the external magnetic field is reduced, the SL magnetization is driven back to its initial state through the restoring effect of IEC or RKKY coupling [25]. Previous studies on SAF-pinned MTJ devices have primarily utilized interlayer exchange coupling to stabilize the reference layer in magnetic-memory applications, thereby minimizing dipolar interaction with the free layer. In contrast, the RKKY-coupled pMTJ proposed in this work employs the coupling as an active restoring mechanism for the storage layer itself. This functional shift transforms the conventional passive pinning role into a dynamic stabilization scheme that enables spin-torque-free, field-driven operation. This mechanism allows rapid recovery between synthetic-ferromagnetic and synthetic-antiferromagnetic states within a few nanoseconds, revealing the physical

basis for the achievable hundreds-of-MHz-level dynamic response discussed in this work. Consequently, the proposed structure bridges memory- and sensor-type MTJs, offering ultrafast recovery while preserving thermal robustness.

As described above, the pMTJ-type TMR sensor exhibits a high sensitivity to variations in the magnetic field while also possessing a natural tendency for the SL magnetization to return to its initial state. To investigate the dynamic response and magnetization behavior of the sensor, micromagnetic simulations are systematically performed. The results reveal that, when the external magnetic field is removed, the SL magnetization relaxes back to its initial state within 1–6 ns depending on the applied magnetic fields. This result suggests that pMTJ-type TMR sensors hold strong potential for applications as high-speed position and angle sensors, as well as in ultrafast leakage current detection.

Finally, magnetic multilayer films were fabricated and optimized to realize the pMTJ-type TMR sensor. To achieve perpendicular magnetic anisotropy, Pt/Co multilayers were employed, while Ru was introduced as an insertion layer to form a synthetic antiferromagnetic (SAF) structure via IEC or RKKY interactions. As a result, the optimal Ru thickness for implementing the pMTJ-type TMR sensor was identified, and a complete magnetic multilayer stack was fabricated to evaluate and verify its performance as a TMR sensor.

2. Sensor Architecture and Working Principle

First, the conventional MRAM architecture is depicted in Figure 1a. It consists of an SL for information retention and an ultrathin MgO tunnel barrier. In this architecture, two RLs are required, which are coupled through a thin IEC or RKKY interaction to form a synthetic antiferromagnetic (SAF) configuration. The role of RL1 is essential, as it completes the magnetic tunnel junction. However, since the RLs are typically composed of Pt/Co multilayers with very strong magnetization, substantial magnetic stray fields are generated. These stray fields induce a shift in the hysteresis loop of the SL. To solve this problem, a much thicker RL2 is introduced so that the stray field from RL2 compensates for that generated by RL1. For this reason, RL2 is often referred to as the shift-canceling layer (SCL).

To adapt the conventional MRAM architecture for use as an ultrasensitive TMR sensor, a modified structure is devised (Figure 1a). The key difference is that the SAF configuration is formed between RL1 and the SL, thereby providing the SL with strong restoring torque. In this scheme, RL2 assumes only the function of the reference layer, which is originally played by RL1 in conventional MRAM. The magnetic multilayer structures employed in this study are shown in Figure 1a. The reference layers are composed of Co/Pt multilayers, while the SL is realized either as a CoFeB single layer or as a Pt/Co/CoFeB multilayer. Ru is used as the insertion layer to induce IEC or RKKY interactions, and the exact SL configuration is determined by the strength of these couplings.

Figure 1b illustrates the operating principle of the modified MRAM-architecture-based TMR sensor. In the initial spin configuration, the two reference layers are aligned parallel to each other, while the SL is antiparallel due to the SAF structure. When an in-plane magnetic field, B_x , is applied, the SL tilts by a finite angle within the plane, and the relative angle between the SL and RL determines the TMR value. In this mode, the device functions as an analog-type TMR sensor. In contrast, when an out-of-plane magnetic field exceeding a certain threshold is applied, magnetization reversal of the SL occurs, and the device operates as a digital-type TMR sensor. Importantly, in both cases, once the external field is removed, the SAF structure provides a strong restoring force, which enables the system to rapidly return to its initial spin configuration. As shown in Figure 1b, under a small in-plane bias field, the SAF alignment exhibits a quasi-linear response due to slight canting of the magnetic moments of SL. This regime can serve as a linear sensing mode, where the resistance change arises from angular deviation between the layers. In this work,

the out-of-plane recovery dynamics are emphasized to demonstrate the ultrafast RKKY-driven stabilization, while the in-plane response confirms the structural versatility of the proposed architecture.

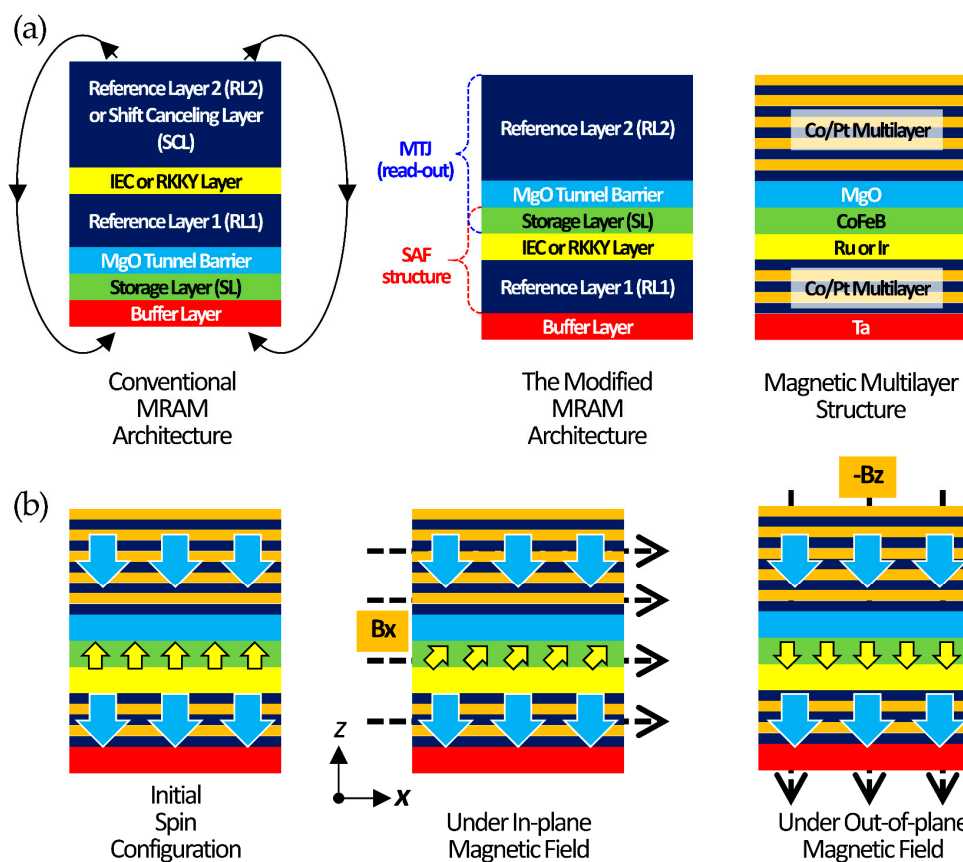


Figure 1. RKKY-pMTJ-based MTJ sensor architecture and working principle: (a) conventional MRAM architecture, the modified MRAM architecture, and magnetic multilayer structure. (b) Initial spin configuration without external field, RKKY-pMTJ-based TMR sensor working principle with in-plane and out-of-plane applied magnetic fields.

3. Experimental Methods

In this study, the multilayer structure of RL1 was designed as $\text{Pt}(4.0)/[\text{Co}(0.6)/\text{Pt}(0.2)]_5$ (units in nm) deposited on a 100 nm-thick thermally oxidized SiO_2 substrate with a Ta (4.0) nm buffer layer. On top of this stack, a wedge-type Ru insertion layer with thickness varying from 0 to 5.6 nm was deposited by using an automatically motorized programmable shadow mask. The multilayer structure of the SL was chosen as $\text{Pt}(0.2)/[\text{Co}(0.6)/\text{Pt}(0.9)]_2/\text{Co}(0.6)/\text{Co}_{20}\text{Fe}_{60}\text{B}_{20}(0.3)$, where the ultrathin CoFeB layer was incorporated to promote MgO deposition and ensure well-matched crystallinity. Since RL2 serves only as the readout element in the RKKY-pMTJ TMR sensor, it was not deposited in this fabrication process, and a Ta (4.0) nm capping layer was placed above the MgO barrier. The base pressure during deposition was maintained at approximately 1×10^{-9} Torr, and the Ar working pressure was fixed at 2 mTorr. All samples are post-annealed at 240 °C for 1 h under an out-of-plane magnetic field of 300 mT.

The next step is to employ magneto-optical Kerr effect (MOKE) spectroscopy to measure the out-of-plane magnetic hysteresis loops as a function of Ru thickness and to determine the corresponding exchange field (H_{ex}) in the SAF structure. The out-of-plane hysteresis loops for varying Ru thicknesses were acquired using a commercial NanoMOKE3 system (Durham Magneto-Optic Ltd., Toft, Cambridge, UK). Figure 2b presents the mag-

netic hysteresis loop of the RKKY-pMTJ-based TMR sensor for the case of $\text{Ru} = 0.6 \text{ nm}$. The red and blue arrows indicate the magnetization orientations of RL1 and SL, respectively. Without external magnetic field in the z -direction, i.e., $H_z = 0 \text{ mT}$, the Kerr signal nearly vanishes because the magnetizations of SL and RL1 are antiparallel, resulting in signal cancelation. This observation confirms the robust formation of the SAF structure.

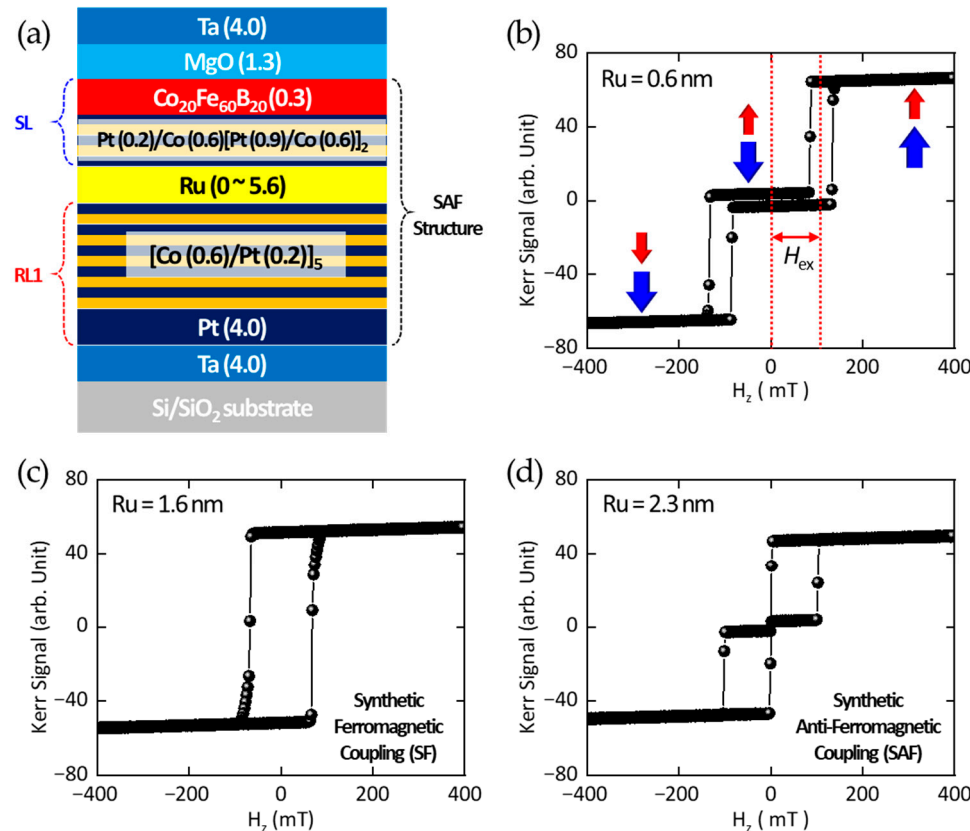


Figure 2. (a) The magnetic multilayer structure of RKKY-pMTJ TMR sensor (thickness in nanometers). (b) The magnetic hysteresis loop of the SAF coupled structure with $\text{Ru} = 0.6 \text{ nm}$. Red and blue arrows indicate the directions of the magnetizations of SL and RL, respectively. The red dotted lines are indicating the exchange field, H_{ex} . (c) The magnetic hysteresis loop of the synthetic ferromagnetically (SF) coupled structure with $\text{Ru} = 1.6 \text{ nm}$. (d) Another SAF coupled structure with $\text{Ru} = 2.3 \text{ nm}$.

4. Results and Discussion

4.1. Magnetic Multilayer Structure for RKKY-pMTJ-Based TMR Sensor

In this subsection, the magnetic multilayer structure of the RKKY-pMTJ-based TMR sensor is introduced. Particular attention is given to the design of RL1 and the SL, and experimental verification is carried out to confirm whether the SAF configuration is established as a function of the Ru insertion layer thickness.

Due to the stray fields originating from RL1 and SL, a difference arises between the switching fields observed during the increasing and decreasing field sweeps in the magnetic hysteresis loops. The arithmetic mean of these two switching fields is defined as the exchange field (H_{ex}). For the case of $H_{\text{ex}} = 0$, the individual magnetic multilayer structures are ferromagnetically coupled, a state referred to as SF coupling. Figure 2c shows the magnetic hysteresis loop measured at a Ru thickness of 1.6 nm, where clear evidence of SF coupling is observed. In contrast, as the Ru thickness is further increased, the SAF configuration reappears. Figure 2d presents the hysteresis loop at a larger Ru thickness, where SAF coupling is observed with $\text{Ru} = 2.3 \text{ nm}$. To ensure reproducibility, each measurement was repeated three times on separate regions of the same sample,

and the variations in coercive and exchange fields were within $\pm 3\%$. The instrumental uncertainty of the MOKE setup was approximately ± 2 mT, and representative data are presented in Figures 2b and 3.

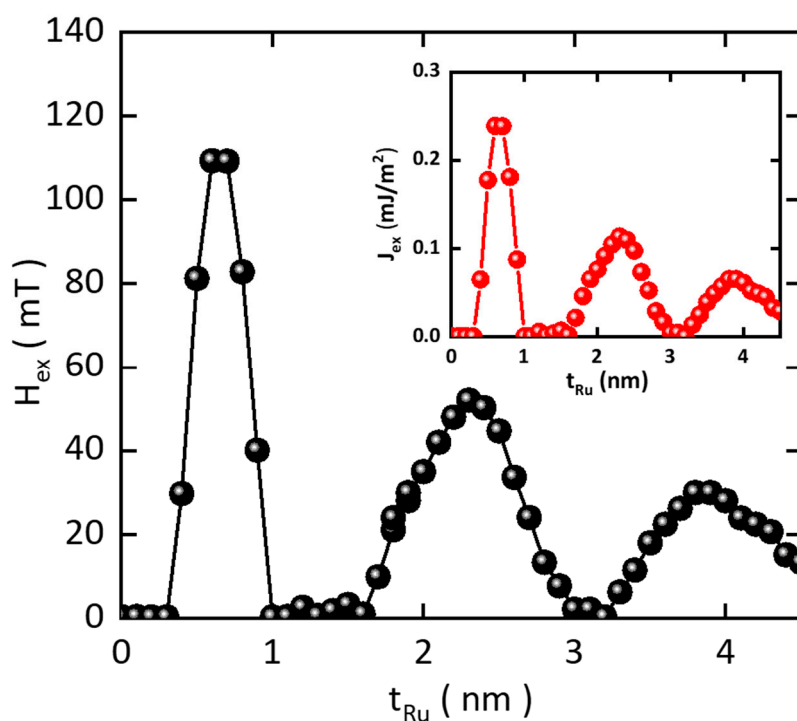


Figure 3. Insertion layer thickness-dependent strength of RKKY interaction, Ru thickness-dependent H_{ex} measurements (Black filled circles) (inset). Conversion curve of H_{ex} to RKKY exchange energy (J_{ex}) (Red filled circles).

4.2. Ru Thickness-Dependent RKKY Interaction and Periodicity Measurements

By employing a wedge-type thin film growth technique with a programmable shadow mask, the dependence of the exchange field (H_{ex}) on the insertion layer (Ru) thickness can be quantitatively examined. Polar MOKE measurements are systematically performed at equally spaced positions using a motorized programmable sample holder, and each hysteresis loop is averaged over more than ten cycles to ensure data reliability. The focused laser spot is translated with a step size of $1\text{ }\mu\text{m}$, corresponding to an incremental Ru thickness of approximately 0.1 nm .

Figure 3 presents the experimental results of H_{ex} as a function of t_{Ru} . The data exhibit a pronounced oscillatory decay with a period of approximately 1.0 nm , showing three well-defined SAF maxima at $t_{\text{Ru}} = 0.6, 2.3$, and 3.9 nm , consistent with earlier reports [26,27]. The maximum exchange field reaches about 110 mT at $t_{\text{Ru}} = 0.6\text{ nm}$. The nearly constant spacing between consecutive maxima— 1.7 nm between the first and second peaks and 1.6 nm between the second and third—indicates that the coupling oscillations are governed by a well-defined electronic structure of Ru. According to the extended theoretical model [28,29], the oscillation period Λ_1 of SAF coupling is given by $2\pi/q_s$, where q_s is the spanning wave vector connecting two antiparallel points on the Fermi surface. The experimentally observed Λ_1 agrees closely with the period predicted from extremal Fermi surface spanning vectors of Ru (0001) [30]. Because Pt and Ru have different crystal structures and distinct Fermi surface topologies, the Λ_1 -periodic coupling cannot propagate effectively through the Pt spacer layer [31].

The interlayer exchange coupling strength J_{ex} is evaluated using the relation [32,33]:

$$J_{\text{ex}} = M_s t H_{\text{ex}}, \quad (1)$$

where M_s is the saturation magnetization, and t is the thickness of the upper ferromagnetic layer [13,14]. The inset of Figure 3 shows J_{ex} as a function of t_{Ru} . With a saturation magnetization of $M_s = 1040 \text{ kA/m}$ (measured by vibrating sample magnetometer, VSM) and a nominal ferromagnetic thickness of $t = 2.1 \text{ nm}$, a strong coupling strength of $J_{\text{ex}} \approx 0.24 \text{ mJ/m}^2$, which is directly proportional to $H_{\text{ex}} \approx 110 \text{ mT}$, is obtained at $t_{\text{Ru}} = 0.6 \text{ nm}$. This confirms that strong and tunable IEC can be achieved by optimizing the Ru thickness, a critical requirement for the stable operation of RKKY-pMTJ-based TMR sensors.

4.3. Structural Analysis of RKKY-pMTJ-Based Ultrafast TMR Sensor via Transmission Electron Microscopy

Finally, the complete magnetic multilayer stack of the RKKY-pMTJ-based TMR sensor architecture (referred to as “the modified MRAM architecture”), including the second reference layer (RL2), is fabricated, and cross-sectional transmission electron microscopy (TEM) is carried out to evaluate the structural quality (Figure 4a). The RL2 structure is designed as $\text{Co}_{20}\text{Fe}_{60}\text{B}_{20}/\text{Ta}/[\text{Co}/\text{Pt}]_3$, as illustrated in Figure 4a. Remarkably, despite the fact that SL, RL1, and RL2 are all based on Pt/Co superlattices, the multilayers exhibit well-defined crystalline ordering. The MgO tunnel barrier also grows uniformly without detectable defects, confirming the robustness of the deposition process.

The full stack comprises three individual magnetic layers that are intricately coupled. Notably, because SL and RL2 are separated by the MgO barrier, a strong IEC is also present across the tunnel barrier. Nevertheless, the magnetic hysteresis loops exhibit well-defined steps and pronounced squareness. This behavior indicates that each of the three magnetic layers retains its distinct functionality within the multilayer architecture while still contributing to the overall stability of the device. The observation of such sharp magnetic transitions demonstrates both the high structural quality of the multilayer films and the effective magnetic decoupling among the layers. Furthermore, the results are consistent with the existence of proximity-induced magnetic moments at the Co/Pt superlattices, which are known to enhance interfacial anisotropy and play a crucial role in stabilizing the perpendicular magnetization of the p-MTJ sensor.

Although this architecture employs a TMR junction for electrical readout, its core functionality is governed by the RKKY-mediated interlayer exchange coupling rather than by the tunnel-barrier transport properties. The storage-layer magnetization is restored by the intrinsic exchange torque, not by spin-transfer or voltage-driven effects, making the TMR ratio and field sensitivity secondary parameters in this proof-of-concept study. The current work therefore focuses on establishing the magnetic stability and dynamic response enabled by RKKY coupling, which define the fundamental operation speed and robustness of the device. For practical implementation, a TMR-based readout structure can be integrated without altering the magnetic design; based on comparable Ta/CoFeB/MgO systems, the expected TMR ratio is $\approx 80\text{--}120\%$, and the field sensitivity $\approx 0.1\text{--}0.2\%/\text{Oe}$ [7,17]. The immediate future work will focus on the microfabrication and electrical characterization of TMR elements using the optimized stack. Direct electrical characterization, including TMR ratio, sensitivity, and linearity range, will be conducted in future work to experimentally validate the device-level performance.

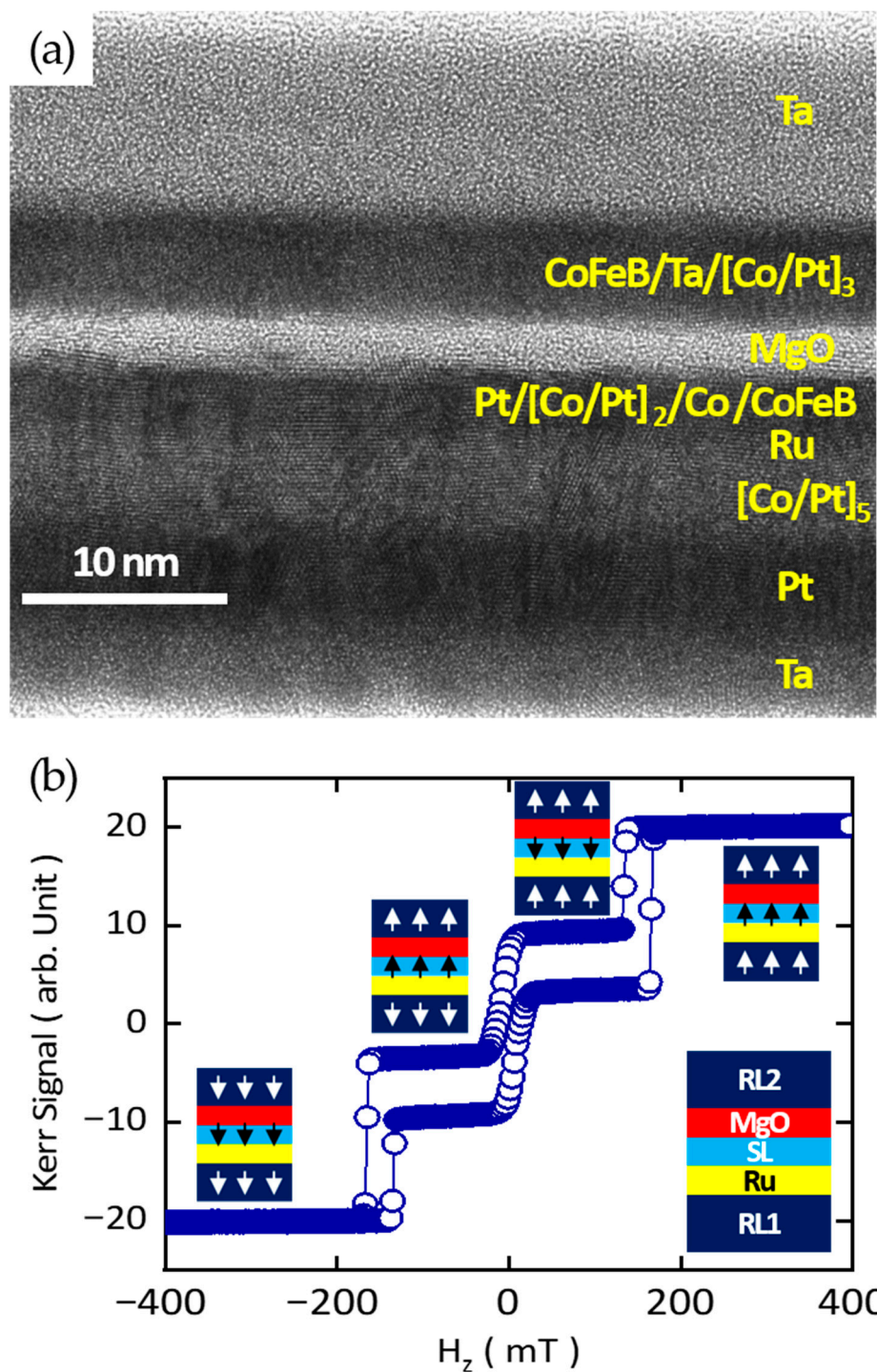


Figure 4. (a) Cross-sectional transmission electron microscopy (image) of RKKY-pMTJ-based ultrafast TMR sensor architecture with full magnetic multilayer stack, (b) polar MOKE measurement as a function of out-of-plane magnetic field (H_z). The full magnetic multilayer stack information and the magnetization configurations of all layers and each step in magnetic hysteresis loop are visualized. White and Black arrows indicate the directions of the magnetizations of RL1, RL2, and SL, respectively.

4.4. Micromagnetic Simulations for Ultrafast TMR Sensor Response: Magnetic Field-Driven SL Reversal and Recovery Time Calculations

In this subsection, micromagnetic simulations are systematically performed to investigate the dynamic response of the RKKY-pMTJ-based TMR sensor. In particular, quantitative calculations are carried out to determine the characteristic switching time required for the sensor to transform from the SAF configuration in its initial equilibrium state to the SF

configuration under the influence of an external magnetic field, as well as the relaxation time needed for the system to return to its initial state once the field is removed. These analyses provide critical insight into the temporal response and stability of the device, which are key performance metrics for high-speed sensor applications.

Figure 5a presents the schematic configuration employed in the modeling. Since the tunnel barrier and RL2 do not directly contribute to the working principle of the sensor, they are excluded from the simulation for computational efficiency and conceptual clarity. Consequently, the modeled structure consists of RL, the insertion layer, and SL, where SL and RL are coupled via RKKY interaction. The finite-difference micromagnetic solver MuMax3 is performed [34], and all material parameters used in the simulations are summarized in Table 1.

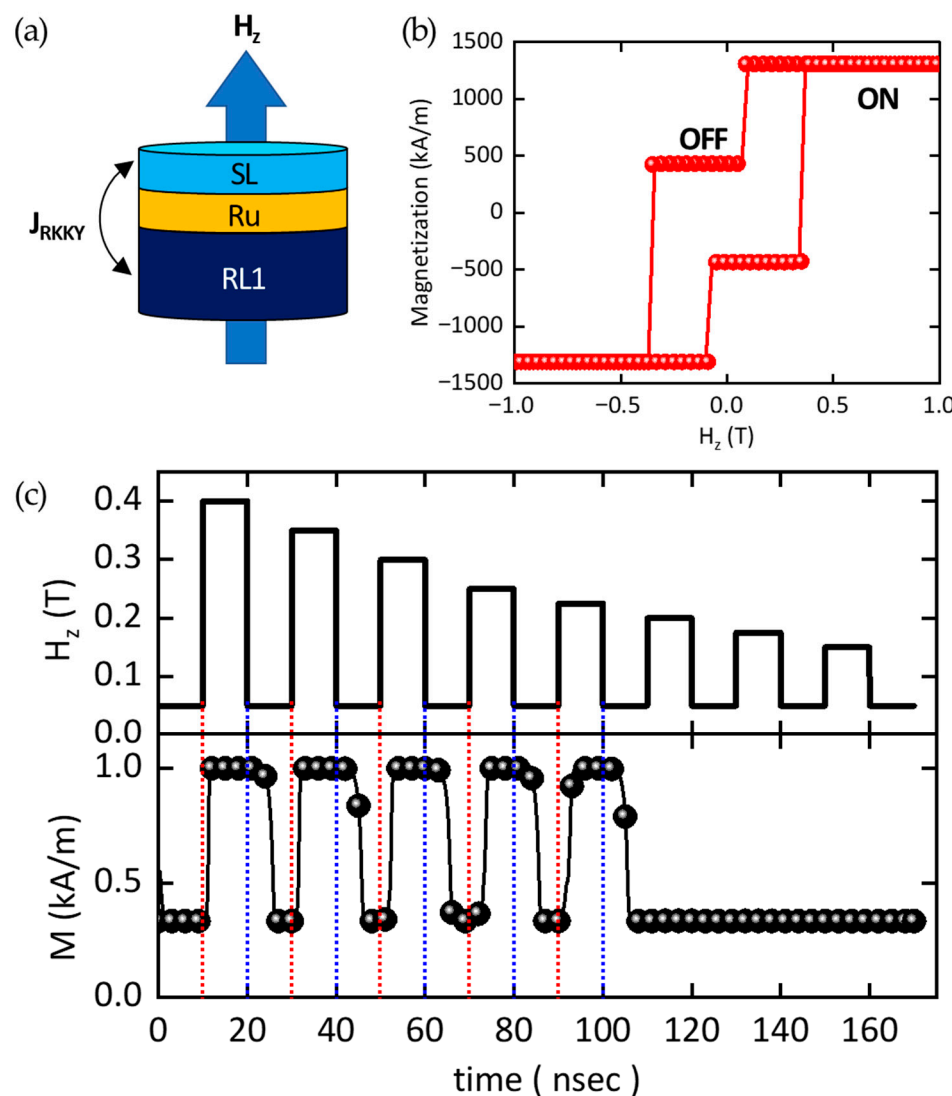


Figure 5. Micromagnetic simulations for ultrafast TMR sensors: (a) Schematic configuration of modeling geometry. J_{RKKY} between SL and RL1 is expressed. (b) Magnetic hysteresis as a function (Red filled circles) of H_z . (c) Top image: the profile of the out-of-plane magnetic field pulse as a function of simulation time (Black solid line). The amplitude of H_z is varied from 0.4 T to 0.15 T with a 0.05 T step. Bottom image: The magnetization profile of the modeling system as a function of simulation time (Black filled circles). The blue and red dashed lines mark the onset and termination of each magnetic field pulse, respectively.

Table 1. Material parameters for micromagnetic simulations.

Material Parameter (Unit)	Reference Layer 1 (RL1)	Storage Layer (SL)
Saturation Magnetization (M_s) (kA/m)	1300	1313
Perpendicular Magnetic Anisotropy Energy Density (K_u) (MJ/m ³)	1300	1300
Exchange Stiffness (A_{ex}) (pJ/m)	15	15
RKKY Exchange Coefficient (J_{RKKY}) (mJ/m ²)		−1.2

In the simulation, both the thickness of RL1 and SL and the interlayer spacing are fixed at 1 nm, while the lateral dimension of each layer is set to 1 $\mu\text{m} \times 1 \mu\text{m}$. A discretization cell size of $1 \times 1 \times 1 \text{ nm}^3$ is employed to ensure accurate resolution of the micromagnetic features. The initial magnetic configuration corresponds to a SAF state, since the interlayer exchange coupling constant is $J_{RKKY} = -1.2 \text{ mJ/m}^2$ (negative sign indicating antiferromagnetic coupling). An external magnetic field is applied in the out-of-plane direction, denoted as H_z .

Figure 5b presents the calculated magnetic hysteresis loop of the modeled system. The magnetization is evaluated while sweeping the external field in increments of 0.01 T (10 mT) in both increasing and decreasing directions. In the initial state, the net magnetization does not converge to zero but stabilizes at approximately 430 kA/m. This residual value originates from the imbalance between the saturation magnetizations of RL1 and SL, combined with the fact that the magnitude of J_{RKKY} is not sufficiently large to enforce perfect compensation. As H_z increases, the magnetization of the SL undergoes reversal, defining the coercive field (H_c), which is determined to be approximately 360 mT.

Finally, the ultrafast switching dynamics of the RKKY-pMTJ-based TMR sensor architecture, hereafter referred to as the modified MRAM structure, are modeled (see Figure 5c). The schematic in the upper panel illustrates the application of an out-of-plane magnetic field pulse. Both the waiting time and the duration time of each pulse are fixed at 10 ns, while the pulse amplitude is systematically reduced from 400 mT in decrements of 50 mT. The simulations are performed down to a pulse amplitude of 150 mT, corresponding to a total simulation time of 170 ns. The blue and red dashed lines mark the onset and termination of each magnetic field pulse, respectively. The “ON” and “OFF” labels indicate the logical states of the TMR sensor corresponding to high- and low-resistance configurations. For the analysis of the simulation results, the operational states of the TMR sensor are defined as follows: (i) During the SAF-to-SF transition, the maximum magnetization reaches approximately 1.0, and the sensor is considered to be in the ‘ON’ state when M_s exceeds 0.9. (ii) During the SF-SAF relaxation process, the minimum magnetization is approximately 0.3, and the sensor is regarded as being in the ‘OFF’ state when M_s falls below 0.4.

Table 2 summarizes the fabrication tolerance and scalability of representative MR sensor technologies, highlighting their underlying magnetic mechanisms and contrasting them with the proposed RKKY-pMTJ architecture. AMR sensors use the anisotropic resistance of NiFe films under magnetization rotation; although easy to fabricate, their performance degrades with pattern size and alignment variation. GMR sensors employ spin-dependent scattering in Co/Cu multilayers, achieving higher output but requiring atomic-scale interface smoothness. TMR sensors utilize quantum tunneling through an MgO barrier between ferromagnetic electrodes, yielding large magnetoresistance yet demanding sub-Å barrier-thickness control. In contrast, the RKKY-pMTJ adopts a perpen-

dicular synthetic–antiferromagnetic structure where the restoring torque originates from interlayer exchange coupling rather than geometric precision or barrier uniformity.

Table 2. Comparison of fabrication tolerance and scalability among MR sensor types.

Sensor Type	Typical Functional Layer (nm)	Thickness Tolerance for Functional Layer (%)	Scaling Potential	Limitation/Advantage
AMR [6]	25	$\pm 10\%$ ($\sim \pm 2.5$ nm)	>1 μm	Signal weakens at nanoscale
GMR [6]	2.0 (spacer layer)	$\pm 5\%$ (± 0.1 nm)	≈ 200 nm	Interface roughness sensitive
In-plane TMR [6]	1.0 (MgO Barrier)	$\pm 3\%$ (± 0.03 nm)	≈ 100 nm	Barrier oxidation
Proposed RKKY-pMTJ	0.6 (Ru layer)	$\pm 17\%$ (± 0.1 nm)	<100 nm	IEC-based self-restoring, robust to scaling

This coupling-driven mechanism allows a broader functional layer thickness margin ($\pm 17\%$, $\approx \pm 0.1$ nm Ru-spacer variation) and supports sub-100 nm device scaling while maintaining thermal stability and ultrafast magnetic recovery. As summarized in Table 2, the RKKY-pMTJ design provides a clear fabrication advantage because its functional stability depends on interlayer coupling rather than on geometric or barrier uniformity. The coupling-based restoring mechanism allows a wider process margin and supports sub-100 nm device scaling, enabling dense integration and consistent performance even under process variation.

From a physical perspective, this modeling framework enables the identification of the critical field amplitude required to trigger reliable magnetization reversal within the SAF-SF transition. The gradual reduction in the pulse amplitude allows one to quantify the threshold field below which the sensor fails to switch within the prescribed timescale. The results highlight the inherent trade-off between switching speed and energy efficiency, since stronger pulses ensure faster transitions, while weaker pulses approach the operational limit of deterministic switching. This analysis therefore provides direct insight into the feasibility of ultrafast operation in practical RKKY-pMTJ-based sensor architectures.

The lower panel of Figure 5c presents the real-time dynamic response of the SL magnetization under applied magnetic field pulses, where the magnetization is recorded with a fixed time step of 0.01 ns (10 ps). Two distinct temporal regimes are particularly relevant for analyzing the magnetization dynamics of the TMR sensor.

In the first regime, corresponding to the onset of a magnetic field pulse, the SL magnetization overcomes the antiferromagnetic interlayer exchange (J_{RKKY}) and attempts to align with the external field direction. The switching time required for this process is defined as $t_{\text{SAF} \rightarrow \text{SF}}$. As expected, stronger field amplitudes result in shorter switching times, since the external torque more efficiently drives the magnetization across the energy barrier imposed by J_{RKKY} coupling. As summarized in Table 3, $t_{\text{SAF} \rightarrow \text{SF}}$ increases gradually from 1.39 ns to 2.94 ns as the field amplitude decreases.

Table 3. Switching times of $t_{\text{SAF} \rightarrow \text{SF}}$ and $t_{\text{SF} \rightarrow \text{SAF}}$ for applying external out-of-plane magnetic field (H_z) pulses.

Switching Time	Hz = 400 mT	350 mT	300 mT	250 mT	200 mT
$t_{\text{SAF} \rightarrow \text{SF}}$	1.39 ns	1.82 ns	2.59 ns	2.90 ns	2.94 ns
$t_{\text{SF} \rightarrow \text{SAF}}$	5.99 ns	5.96 ns	5.91 ns	5.84 ns	5.78 ns

In the second regime, corresponding to the termination of the magnetic field pulse, the system undergoes a relaxation process that restores the initial SAF configuration. The characteristic time of this process, $t_{SF \rightarrow SAF}$, exhibits an intriguing trend: it decreases slightly as the field amplitude is reduced. This behavior arises because weaker field amplitudes produce a smaller net magnetization in the transient SF state, thereby lowering the effective relaxation energy barrier. Nevertheless, the variation of $t_{SF \rightarrow SAF}$ is relatively small, ranging only from 5.99 ns to 5.78 ns, indicating that the recovery dynamics are largely governed by the intrinsic interlayer exchange field rather than the external field history. Also, it is noteworthy that the amplitudes of the magnetic field pulses are insufficient to trigger the SAF-SF transition when the applied magnetic field amplitude is below 200 mT (See Figure 5c). The relaxation time $t_{SF \rightarrow SAF}$ extracted from micromagnetic simulations is approximately 5.8–6.0 ns, representing the interval required for the storage-layer magnetization to return from the transient synthetic–ferromagnetic state to the synthetic–antiferromagnetic equilibrium after the external field pulse is removed. This timescale sets the intrinsic response limit of the RKKY-coupled pMTJ element. By taking $f \approx 1/t_{SF \rightarrow SAF}$, the corresponding characteristic frequency is on the order of 1.7×10^8 s⁻¹ (≈ 170 MHz). This indicates that the proposed architecture can in principle sustain sub-10 ns, self-restoring operation driven purely by interlayer exchange coupling. We note that this value reflects the device-level magnetic dynamics of the multilayer stack itself.

From a physical perspective, these findings highlight the asymmetric nature of field-driven switching and relaxation processes in the RKKY-pMTJ architecture. While the forward transition (SAF \rightarrow SF) is strongly field-dependent, the backward recovery (SF \rightarrow SAF) is primarily stabilized by intrinsic coupling, ensuring robust return to the equilibrium configuration. This asymmetry underlines both the ultrafast responsiveness and inherent stability of the proposed sensor architecture.

5. Conclusions

In summary, this research validates the RKKY-pMTJ as a transformative pathway for magnetic sensing. The comprehensive study first established the structural integrity and magnetic coupling of the multilayer stack via TEM and MOKE analyses, pinpointing the 0.6 nm Ru interlayer as optimal for maximum SAF strength. This foundational work ensured the material system possessed the necessary thermal robustness and strong IEC needed for deterministic operation. Subsequently, dynamic micromagnetic simulations provided definitive proof of concept, showing that the RKKY-stabilized SL magnetization rapidly returns to its stable state in less than 6 ns. This ultrafast recovery and the inherent stability derived from the internal RKKY restoring force represent a significant scientific achievement in high-speed spintronic sensor design. The successful demonstration of a design principle that decouples high-speed operation from dependence on complex external control signals marks a major advancement in the field. In addition to these qualitative findings, this study quantitatively confirmed an RKKY exchange energy of approximately 0.24 mJ/m² at a Ru-spacer thickness of 0.6 nm through systematic IEC analysis. Micromagnetic simulations further verified that the storage-layer magnetization returns to the synthetic–antiferromagnetic equilibrium within ≈ 6 ns, corresponding to an intrinsic operational frequency approaching 200 MHz. These results provide strong evidence that the proposed RKKY-pMTJ architecture can achieve ultrafast, spin-torque-free response while maintaining thermal robustness, demonstrating a clear performance advantage over conventional in-plane TMR sensors.

The immediate future work will focus on the microfabrication and electrical characterization of TMR elements using the optimized stack. This crucial phase involves evaluating key electrical metrics—specifically the TMR ratio and sensor linearity—under various

conditions. Most critically, robust performance must be validated across a wide range of temperatures through thermal cycling tests (e.g., -40°C to $+80^{\circ}\text{C}$) to confirm commercial viability. Successful execution will pave the way for the deployment of these scalable, GHz-capable sensors for advanced electric vehicle and factory automation systems.

In future work, it will be necessary to fabricate a sub-100 nm-scale RKKY-pMTJ-based TMR sensor array, followed by full packaging with top and bottom electrodes, in order to systematically evaluate the electrical and magnetic properties of the TMR sensor devices.

Author Contributions: Conceptualization, J.-S.K.; data curation, J.C.; funding acquisition, J.-S.K.; investigation, J.C. and J.-S.K.; methodology, J.C. and J.-S.K.; project administration, J.-S.K.; supervision, J.-S.K.; visualization, J.C. and J.-S.K.; writing—original draft, J.C. and J.-S.K.; writing—review and editing, J.C. and J.-S.K. All authors will be updated at each stage of manuscript processing, including submission, revision, and revision reminder, via emails from our system or the assigned Assistant Editor. All authors have read and agreed to the published version of the manuscript.

Funding: This work has been supported by the National Research Foundation of Korea (NRF) and funded by the Ministry of Science and ICT (2021M3F3A2A01037526) and the DGIST R&D Programs (25-ET-02, 25-SENS-01, and 25-SENS2-11).

Institutional Review Board Statement: Not applicable.

Informed Consent Statement: Not applicable.

Data Availability Statement: The data that support the findings of this study are available from the corresponding author upon reasonable request.

Acknowledgments: The authors would like to thank the editors and anonymous reviewers. Special gratitude is given to all project team members for their contributions to this study.

Conflicts of Interest: The authors declare no conflicts of interest.

References

1. Vaheeda, J.T.; George, B. TMR Sensor-Based Detection of EVs in Semi-Dynamic Traffic for Optimal Charging. *IEEE Trans. Intell. Transp. Syst.* **2022**, *23*, 13721–13730. [[CrossRef](#)]
2. Liu, X.; Liu, C.; Han, W.; Pong, P.W.T. Design and Implementation of a Multi-Purpose TMR Sensor Matrix for Wireless Electric Vehicle Charging. *IEEE Sens. J.* **2019**, *19*, 1683–1692. [[CrossRef](#)]
3. Liu, X.; Liu, C.; Pong, P.W.T. TMR-Sensor-Array-Based Misalignment-Tolerant Wireless Charging Technique for Roadway Electric Vehicles. *IEEE Trans. Magn.* **2019**, *55*, 4003107. [[CrossRef](#)]
4. Nandapurkar, K.B.; Sreekantan, A.C.; Dutta, P.K. Performance Investigation of a Simplified TMR-Based Rotary Position Sensing System. *IEEE Trans. Inst. Meas.* **2021**, *70*, 9505408.
5. Ranjan, R.; Shekhar, A.; Manda, S. Development of a Tunneling Magneto-Resistance Sensor Based Orientation Detection System for Robotic Manipulator. In Proceedings of the 2025 6th International Conference on Recent Advances in Information Technology (RAIT), Dhanbad, India, 6–8 March 2025.
6. Khan, M.A.; Sun, J.; Li, B.; Przybysz, A.; Kosel, J. Magnetic sensors—A review and recent technologies. *Eng. Res. Express* **2021**, *3*, 022005.
7. Wiśniowski, P.; Nawrocki, M.; Wrona, J.; Cardoso, S.; Freitas, P.P. Bias Voltage Dependence of Sensing Characteristics in Tunneling Magnetoresistance Sensors. *Sensors* **2021**, *21*, 2495. [[CrossRef](#)] [[PubMed](#)]
8. Jin, Z.; Sam, M.A.I.M.N.; Oogane, M.; Ando, Y. Serial MTJ-Based TMR Sensors in Bridge Configuration for Detection of Fractured Steel Bar in Magnetic Flux Leakage Testing. *Sensors* **2021**, *21*, 668. [[CrossRef](#)]
9. Ikegawa, S.; Mancoff, F.B.; Janesky, J.; Aggarwal, S. Magnetoresistive Random Access Memory: Present and Future. *IEEE Trans. Electron. Devices* **2020**, *67*, 1407–1419. [[CrossRef](#)]
10. Ohno, H.; Endoh, T.; Hanyu, T.; Ando, Y.; Ikeda, S. Spin-transfer-torque magnetoresistive random access memory (STT-MRAM) technology. In *Book Advances in Non-Volatile Memory and Storage Technology*, 1st ed.; Nishi, Y., Ed.; Woodhead Publishing: Cambridge, UK, 2014; pp. 455–494.
11. Cho, J.; Kim, N.-H.; Lee, S.; Kim, J.-S.; Lavrijsen, R.; Solignac, A.; Yin, Y.; Han, D.-S.; van Hoof, N.J.J.; Swagten, H.J.M.; et al. Thickness dependence of the interfacial Dzyaloshinskii–Moriya interaction in inversion symmetry broken systems. *Nat. Commun.* **2015**, *6*, 7635. [[CrossRef](#)]

12. Jung, J.; Cho, J.; Choi, H.-C.; Lee, K.; You, C.-Y.; Choe, S.-B.; Kim, J.-S. Modulations of interfacial magnetic properties using structurally inverted magnetic tri-layer systems: Toward skyrmion formation. *Appl. Phys. Lett.* **2021**, *118*, 262408. [\[CrossRef\]](#)

13. Cho, J.; Jung, J.; Kim, S.B.; Ju, W.R.; Kim, D.H.; Byun, M.; Kim, J.-S. The Stack Optimization of Magnetic Heterojunction Structures for Next-Generation Spintronic Logic Applications. *Materials* **2023**, *16*, 6418. [\[CrossRef\]](#)

14. Cho, J.; Lee, C.-K.; Kim, J.; Kim, J.-S.; You, C.-Y. The sign of the interfacial Dzyaloshinskii–Moriya interaction in ultrathin amorphous and polycrystalline magnetic films. *J. Phys. D Appl. Phys.* **2022**, *55*, 435008. [\[CrossRef\]](#)

15. Liu, Y.; Qiu, J.; Lim, Z.T.; Toh, S.L.; Zhu, Z.; Han, G.; Zhu, K. Strong perpendicular magnetic anisotropy in $[Co/Pt]_n$ ultrathin superlattices. *Appl. Phys. Expr.* **2017**, *10*, 013005. [\[CrossRef\]](#)

16. Yakushiki, K.; Saruya, T.; Kubota, H.; Fukushima, A.; Nagahama, T.; Yuasa, S.; Ando, K. Ultrathin Co/Pt and Co/Pd superlattice films for MgO-based perpendicular magnetic tunnel junctions. *Appl. Phys. Lett.* **2010**, *97*, 232508. [\[CrossRef\]](#)

17. Ikeda, S.; Miura, K.; Yamamoto, H.; Mizunuma, K.; Gan, H.D.; Endo, M.; Kanai, S.; Hayakawa, J.; Matsukura, F.; Ohno, H. A perpendicular-anisotropy CoFeB–MgO magnetic tunnel junction. *Nat. Mater.* **2010**, *9*, 721–724. [\[CrossRef\]](#)

18. Yen, Y.-S.; Yang, C.-L.; Chang, Y.-L.; Lai, C.-H. Optimizing Perpendicular Magnetic Anisotropy in MgO/CoFeB Structures Through Ultrathin CoFeB-Enhanced Ta Capping Layers. *ACS Omega* **2025**, *10*, 18510–18516. [\[CrossRef\]](#)

19. Li, Z.-P.; Li, S.; Zheng, Y.; Fang, J.; Chen, L.; Hong, L.; Wang, H. The study of origin of interfacial perpendicular magnetic anisotropy in ultra-thin CoFeB layer on the top of MgO based magnetic tunnel junction. *Appl. Phys. Lett.* **2016**, *109*, 182403. [\[CrossRef\]](#)

20. Chiou, J.-Y.; Chang, H.W.; Chi, C.-C.; Hsiao, C.-H.; Ouyang, C. L_{10} FePt Films with Optimal (001) Texture on Amorphous SiO₂/Si Substrates for High-Density Perpendicular Magnetic Recording Media. *ACS Appl. Nano Mater.* **2019**, *2*, 5663–5673. [\[CrossRef\]](#)

21. Lee, H.-R.; Lee, K.; Cho, J.; Choi, Y.-H.; You, C.-Y.; Jung, M.-H.; Bonell, F.; Shiota, Y.; Miwa, S.; Suzuki, Y. Spin-orbit torque in a bulk perpendicular magnetic anisotropy Pd/FePd/MgO system. *Sci. Rep.* **2014**, *4*, 6548. [\[CrossRef\]](#)

22. Nishioka, K.; Honjo, H.; Ikeda, S.; Watanabe, T.; Miura, S.; Inoue, H.; Tanigawa, T.; Noguchi, Y.; Yasuhira, M.; Sato, H.; et al. Novel Quad-Interface MTJ Technology and Its First Demonstration with High Thermal Stability Factor and Switching Efficiency for STT-MRAM Beyond 2X nm. *IEEE Trans. Electron. Devices* **2020**, *67*, 995–1000. [\[CrossRef\]](#)

23. Liu, E.; Swerts, J.; Wu, Y.C.; Vayset, A.; Couet, S.; Mertens, S.; Rao, S.; Kim, W.; Elshocht, S.V.; Boeck, J.D.; et al. Top-Pinned STT-MRAM Devices with High Thermal Stability Hybrid Free Layers for High-Density Memory Applications. *IEEE Trans. Magn.* **2018**, *54*, 3401805. [\[CrossRef\]](#)

24. Huai, Y.; Gan, H.; Wang, Z.; Xu, P.; Hao, X.; Yen, B.K.; Malmhall, R.; Pakala, N.; Wang, C.; Zhang, Z.; et al. High performance perpendicular magnetic tunnel junction with Co/Ir interfacial anisotropy for embedded and standalone STT-MRAM applications. *Appl. Phys. Lett.* **2018**, *112*, 092402. [\[CrossRef\]](#)

25. Gan, H.; Malmhall, R.; Wang, Z.; Yen, B.K.; Zhang, J.; Wang, X.; Zhou, Y.; Hao, X.; Jung, D.; Satoh, K.; et al. Perpendicular magnetic tunnel junction with thin CoFeB/Ta/Co/Pd/Co reference layer. *Appl. Phys. Lett.* **2014**, *105*, 192403. [\[CrossRef\]](#)

26. Parkin, S.S.P.; More, N.; Roche, K.P. Oscillations in exchange coupling and magnetoresistance in metallic superlattice structures: Co/Ru, Co/Cr, and Fe/Cr. *Phys. Rev. Lett.* **1990**, *64*, 2304. [\[CrossRef\]](#)

27. Bandiera, S.; Sousa, R.C.; Auffret, S.; Rodmacq, B.; Dieny, B. Enhancement of perpendicular magnetic anisotropy thanks to Pt insertions in synthetic antiferromagnets. *Appl. Phys. Lett.* **2012**, *101*, 072410. [\[CrossRef\]](#)

28. Bruno, P. Theory of interlayer exchange interactions in magnetic multilayers. *J. Phys. Condens. Matter* **1999**, *11*, 9403. [\[CrossRef\]](#)

29. Yafet, Y. Ruderman–Kittel–Kasuya–Yosida range function of a one-dimensional free-electron gas. *Phys. Rev. B* **1987**, *36*, 3948. [\[CrossRef\]](#) [\[PubMed\]](#)

30. Stiles, M.D. Exchange coupling in magnetic heterostructures. *Phys. Rev. B* **1993**, *48*, 7238. [\[CrossRef\]](#) [\[PubMed\]](#)

31. Saito, Y.; Ikeda, S.; Endoh, T. Synthetic antiferromagnetic layer based on Pt/Ru/Pt spacer layer with 1.05 nm interlayer exchange oscillation period for spin–orbit torque devices. *Appl. Phys. Lett.* **2021**, *119*, 142401. [\[CrossRef\]](#)

32. Bloemen, P.J.H.; Vankesteren, H.W.; Swagten, H.J.M.; Dejongs, W.J.M. Oscillatory interlayer exchange coupling in Co/Ru multilayers and bilayers. *Phys. Rev. B* **1994**, *50*, 13505. [\[CrossRef\]](#)

33. Folkerts, W. Calculated magnetic phase diagrams and magnetoresistance curves for an antiferromagnetically coupled multilayer system. *J. Magn. Magn. Mater.* **1991**, *94*, 302. [\[CrossRef\]](#)

34. Vansteenkiste, A.; Leliaert, J.; Dvornik, M.; Helsen, M.; Garcia-Sanchez, P.; Waeyenberge, B.V. The design and verification of MuMax3. *AIP Adv.* **2014**, *4*, 107133. [\[CrossRef\]](#)